NREL/TP-257-4654 • UC Category: 261 • DE92001200

Recent Results from Data Analysis of Dynamic Stall on Wind Turbine Blades

C.P. Butterfield
D. Simms
National Renewable Energy Laboratory

Dr. S. Huyer
University of Colorado

Presented at the International Energy Agency Experts Meeting on Wind Turbine Aerodynamics, Stuttgart, Germany, December 3-4, 1991

National Renewable Energy Laboratory
(formerly the Solar Energy Research Institute)
1617 Cole Boulevard
Golden, Colorado 80401-3393
A Division of Midwest Research Institute
Operated for the U.S. Department of Energy
under Contract No. DE-AC02-83CH10093

January 1992

On September 16, 1991, the Solar Energy Research Institute was designated a national laboratory, and its name was changed to the National Renewable Energy Laboratory.

NOTICE

Printed in the United States of America
Available from:
National Technical Information Service
U.S. Department of Commerce
5285 Port Royal Road
Springfield, VA 22161

Price: Microfiche A01
Printed Copy A03

Codes are used for pricing all publications. The code is determined by the number of pages in the publication. Information pertaining to the pricing codes can be found in the current issue of the following publications which are generally available in most libraries: *Energy Research Abstracts (ERA)*; *Government Reports Announcements* and Index (*GRA* and I); *Scientific and Technical Abstract Reports (STAR)*; and publication NTIS-PR-360 available from NTIS at the above address.

Recent Results from Data Analysis of Dynamic Stall on Wind Turbine Blades

C.P. Butterfield (NREL*)
Dr. S. Huyer (University of Colorado)
D. Simms (NREL)

*** National Renewable Energy Laboratory (NREL), formerly the Solar Energy Research Institute (SERI)**

Presented at the International Energy Agency Experts Meeting on Wind Turbine Aerodynamics Stuttgart, Germany December 3-4, 1991

Abstract

Wind turbines are subjected to dynamic loading from a variety of different sources. Wind shear and turbulence cause time-varying inflow that results in unsteady airloads. Tower shadow, upwind turbine wakes, and yaw angles also introduce unsteady inflow to wind turbine rotors. Wind turbine designers must predict these loads accurately in order to adequately design blades, hubs, and the remaining support structure to achieve a 30-year life. Structural analysts have not been able to predict mean or dynamic loads accurately enough to predict the fatigue life of major wind turbine components with confidence. Part of the problem is due to uncertainty in the stochastic wind environment as mentioned earlier. Another important part of the problem is the lack of basic knowledge of rotary wing airfoil stall performance. There is mounting evidence that dynamic stall may be related to dynamic loads that are greater than predictions. This paper describes some results of investigations of unsteady aerodynamic loads measured on a wind turbine blade. The objective of the investigation is to understand the steady and unsteady stall behavior of wind turbine blades.

Introduction

The helicopter industry has invested significant research time in understanding dynamic stall on helicopter blades but has ignored steady stall because helicopters avoid operating conditions that would result in large-scale steady stall. Wind turbines commonly operate in steady stall as a means of regulating peak power and loads. It has been discovered by Butterfield et al. [1] and many others [2,3] that airfoils do not stall on rotating wings as they do in wind tunnel tests. Butterfield et al. [4] also discovered that dynamic stall can exist on wind turbine blades during normal operating conditions. There is mounting evidence that dynamic stall may be related dynamic loads that are greater than predictions. Wright [5] and Hansen [6] show improved accuracy in predicted dynamic loads and yaw loads when dynamic stall is introduced into their dynamic analyses.

In order to develop static and dynamic stall models for wind turbines, a data base of measured dynamic stall characteristics must exist for comparison and validation of new codes. Helicopter experience and codes may be applicable but must be validated using measurements from operating wind turbine measurements. The National Renewable Energy Laboratory (NREL), supported by the U.S. Department of Energy (DOE), has conducted a series of experiments that will supply this basic data. The experiment is called the Combined Experiment and is described by Butterfield et al. in two references [7,8]. This paper describes dynamic stall measurements at four blade spanwise stations of a rotating wind turbine blade. Loads are correlated with the measured airloads. Time-varying pressure distributions are examined in detail.

Test Description

A 10-m, three bladed, downwind horizontal axis wind turbine was used as a test platform. Molds were made to high tolerances so that airfoil coordinates would be accurately transferred to the test blades. The NREL S809 airfoil was used because extensive wind tunnel data were available for this airfoil. This airfoil is one of a family of airfoils designed specifically for wind turbine use. Tangler [9] describes the airfoil as a 21% thick, laminar flow airfoil with low roughness sensitivity.

Two blades were made with no instrumentation; a third was constructed with 124 pressure taps installed inside the blade. Butterfield [7] describes the installation technique and the pressure measurement instrumentation for the first phase of this test program. Phase II testing required four chordwise pressure distributions located at 30%, 47%, 63%, and 80% blade spans. Pressure taps were located at 4% chord and 36% chord on the suction side of the airfoil, for six additional spanwise locations.

These pressure tap locations and instrumentation were used in wind tunnel tests at the Ohio State University (OSU) and Colorado State University (CSU) wind tunnels as described by Butterfield et al. [12]. By keeping the instrumentation, pressure tap, and airfoil identical between wind tunnel tests and rotating blade wind turbine tests, differences in the results would be more likely attributable to real differences in airfoil performance caused by three-dimensional and rotating blade effects.

The dynamic pressure and local flow angle were measured at each of the four pressure distributions. Dynamic pressure was measured using a total pressure probe with an internal angle of 45 deg. This probe was tested in the CSU wind tunnel and found to give accurate total pressure measurements for angular misalignments up to 40 deg. The flow angle probe was also tested in the wind tunnel while mounted on the airfoil. Up-wash caused by circulation effects causes local flow angles to deviate from the geometric angle of attack. In this test the deviations were measured and used to correct the rotating blade measured angles. Butterfield [4] describes these corrections as well as dynamic response tests performed on the probe. Total pressure (dynamic pressure) measured by the probe was not affected by up-wash.

Data Case Descriptions

Two data cases were chosen for analysis of results shown in figures 1 through 22. The first case spanned 20 s of time during 30-deg yaw angle operation and wind speeds of 13.5 m/s. The compass yaw angle of the turbine was 300 deg while the wind direction was 270 deg. The turbine rotates clockwise when viewed from a downwind location looking into the wind. The instrumented blade is pointing up when in the 0-deg azimuth position.

The second case spanned 10 s of time during zero yaw error in wind speeds of 15 m/s. These two cases are compared in Table 1 and were chosen to illustrate the conditions that cause dynamic stall.

Table 1. Comparison of Two Data Cases

	30-deg Yaw Case	No Yaw Case
Vertical Plane Array (VPA) Average Wind Speed (m/s)	13.67	15.39
Average Turbine Intensity	0.14	0.06
Shear (m/s)	1.24	0.72
Pitch Angle (deg)	11.3	11.54
Pitch Standard Deviation (deg)	0.33	0.21
Rotor Torque (N-m)	1392	1976

Data Processing and Pressure Coefficient Normalization

All the pressure data were digitized at a 520-Hz sample rate. Data were later filtered at 10-Hz and pre-averaged by a factor of 10 to obtain a final 10-Hz bandwidth and 52-Hz sample rate. These data were then sorted into bins using the measured angle of attack (AOA) as the independent variable. This approach was used for results presented in figures 1 through 22.

To obtain normalized pressure coefficients, dimensional pressure data were divided by local dynamic pressure per equation (1). Dynamic pressure was established in two ways. First, atmospheric pressure was subtracted from measured total pressure to get a local dynamic pressure (Q). The second method derived the local value of Q by using equation (2) plus the disk-averaged wind speed (measured from the vertical plane array), the rotor angular speed, and the radius to the pressure tap.

$$C_P = (P_{surface} - P_{atm}) / Q \quad (1)$$

$$Q = 1/2 \text{ (density) } (\text{(wind speed)}^2 + (r * \text{omega})^2) \quad (2)$$

Both methods gave similar results for small yaw angles. This was demonstrated by Butterfield et al. [12] when both normalization techniques compared well with wind tunnel data at low AOAs. At high AOAs (greater than 25 deg), the measured Q method gave values of pressure coefficient (Cp) greater than one for the 30% blade span pressure distribution.

Most wind tunnel dynamic stall data are normalized by local dynamic pressure. This is simple because dynamic pressure in the wind tunnel is steady. These data are then used by structural dynamic codes, using unsteady local dynamic pressure to calculate blade forces. Figure 1 shows measured and calculated dynamic pressure during yawed operation. The measured dynamic pressure (Q) shows the tower shadow at approximately 180 deg. The calculations included the vector sum of the free stream velocity and the in-plane blade velocity component, which included the effects of the advancing and retreating blade in yawed flow. Figure 2 shows lift coefficient dynamic stall with constant Q (uncorrected), calculated per equation 2, and time varying Q (corrected) as shown in Figure 2. The corrected curve is the appropriate curve for structural dynamic codes, which calculate local, time-varying Q. This indicates that the effects of dynamic stall can appear to be more severe or less severe depending on the normalization used.

For spanwise airloads it is appropriate to normalize by the dynamic pressure calculated at the blade tip. This approach shows a more realistic full blade load distribution. In this report all data are normalized by local dynamic pressure based on the free-stream velocity (as in equation 2) except spanwise pressure distributions presented in the pressure distributions section. These are normalized by blade tip dynamic pressure.

Azimuth-Averaged Results

Figures 3 through 6 illustrate AOA and lift coefficient (C_L) variations azimuth averaged over 25 revolutions during 30-deg yawed operation for 80%, 63%, 47%, and 30% blade spans. The inboard stations clearly reach high values of C_{Lmax} while the blade is rising at azimuth angles of 270 deg. Minimum values of C_L occur after the airfoil has stalled, when the blade azimuth angle is between 0 and 90 deg, on the downwind side of the rotor. Static stall in wind tunnel tests results in values of C_{Lmax} equal to 0.95. If the airfoil did not stall and was linearly related to AOA, the C_L would follow the AOA in the cosine shape shown in the same figures. The difference in lift that exists from the upwind side of the yawed rotor (200 to 300 deg azimuth angle) to the downwind side of the rotor (0 to 100 deg azimuth angle) causes high yaw moments and low speed shaft (LSS) cyclic loads.

Peak-to-peak values of AOA vary from 11 deg at the 80% span to 26 deg at the 30% span. This implies that all horizontal-axis rotors would experience AOA cyclic amplitudes large enough to cause dynamic stall for even modest yaw angles. Both fixed-pitch rotors and partially feathered pitch-control rotors would experience maximum AOAs great enough to cause local stalling.

Figures 7 through 10 show similar plots of C_L and AOA variations during 0-deg yaw error operation. As can be seen for this case, AOA variations are small by comparison because asymmetrical inflow is due only to wind shear of 0.7 m/s across the rotor. Tower shadow is the major contributor to inflow disturbances. This is obvious from the rapid change in AOA and C_L at 180-deg azimuth angle. This disturbance is large enough to cause dynamic stall as implied by the sudden rise in C_L above static stall C_{Lmax} of 0.95.

Dynamic Stall Results

Figures 11 through 14 illustrate azimuth-averaged C_L versus AOA compared to static lift curves measured in the CSU wind tunnel tests [12]. The dynamic stall behavior is evident in the large hysteresis loops that surround the static curves. At the 80% span the rotating blade C_{Lmax} values do not exceed static values significantly. Conversely, Figures 12 through 14 show stations 63%, 47%, and 30%, which show C_{Lmax} values exceeding static values by 32% to 110%, respectively. The labeled center symbols indicate blade azimuth angle. The difference in lift at azimuth angles of 90 deg and 270 deg is again obvious in these curves. As the hysteresis loops grow larger, the differences increase and the resulting yaw moments increase.

Pressure Distributions

Figure 15 shows the upper surface pressure distribution of a rotating turbine blade with zero yaw taken at 30% span at a wind velocity of 14.7 m/s over a single rotational cycle. At 0-deg azimuth, the turbine blade is pointing up and at 180 deg the blade is in the center of the wake behind the tower. Three-dimensional surface plots illustrate the chordwise pressure distribution and its variation throughout the rotation cycle. At stations downstream along the chord, a delay in suction pressure maxima occurred relative to the rotation cycle. Robinson [13] used flow visualization in conjunction

with surface pressure data to correlate dynamic stall vortex formation with unsteady surface pressure signatures. He observed a temporal delay in maximum suction pressure at downstream locations along the chord, which corresponded to passage of a dynamic stall vortex. Present results seem consistent with vortex formation and convection over the suction surface of wind turbine blades. This pressure signature becomes more obvious for a yawed horizontal axis wind turbine (HAWT) as will be demonstrated later.

Figure 16 shows a comparison of measured and theoretical AOA. The agreement is generally good but there are discrepancies at high AOAs and the transducer cannot respond fast enough to characterize the tower shadow. The discrepancy at high angles may be due to induced velocity effects or flow anomalies that are not included in the theoretical curve. The theoretical model only includes the vector addition of free-stream velocity, local in-plain velocity, the effect of the yawed turbine and a simple tower shadow model. This comparison demonstrates that the measured AOA yields reasonable results and has sufficient frequency response to give accurate dynamic stall characterization for yawed flow conditions but not for tower shadow comparisons.

Figure 17 shows the theoretical AOA variation of a yawed downstream HAWT for a yaw angle of 30 deg and wind velocity of 16.7 m/s. Figure 18 shows a bin-averaged upper surface pressure distribution at 30% span for 30-deg yaw. This may be contrasted to single cycle data shown in Figure 19 for similar test conditions. In both cases, two suction pressure peaks were seen. Data taken for a single cycle, however, shows that the suction pressure peaks are larger and more transient in nature. Convection of a vortex structure may be inferred by the delay in maximum suction pressure at downstream stations along the chord, which is consistent with results seen for pitching airfoils.

Figure 20 shows the upper surface pressure distribution for a turbine blade situated at -33-deg yaw over one cycle. Notice that the suction pressure peaks are approximately 180 deg out of phase compared with the positive yaw case. Four discrete suction pressure peaks were observed, implying the formation of a number of vortices throughout the rotation cycle. Convection of these vortices may be inferred at both 75-deg and 270-deg azimuth. The upper surface pressure distribution at 63% span is shown in Figure 21. A suction pressure spike was observed at approximately 120-deg azimuth and a smaller spike at 210 deg. Notice that the suction pressure peak persists over a larger portion of the cycle (90-120 deg) and convection of this vortex can be inferred in the suction pressure ridge, but only up to 50% chord. This is in contrast to well defined vortex convection to the trailing edge at 30% span.

Figures 22 and 23 show spanwise pressure distributions taken at the 4% chord location for 0-deg yaw and bin-averaged results. All spanwise pressures were normalized with respect to the tip velocity using $Q = 1/2\ \rho * (V^2 + R\omega^2)$ where R = 5.05 m. As can be seen in Figure 22, for low wind velocities of 7.7 m/s, surface pressure remains approximately constant along the span. There does appear a suction pressure maximum at approximately 47% span with suction pressure decreasing modestly inboard and outboard. This may be contrasted with the high wind velocity case of 18.7 m/s seen in Figure 23. For this case, suction pressure decreases slightly from 30% to 47% span and little evidence of a tower shadow induced vortex can be seen. From 50% span outboard, however, overall suction pressure increases appreciably. In addition, a tower shadow induced vortex signature becomes more well defined at 180-deg azimuth for outboard stations.

Figures 24 and 25 show surface pressure distributions taken at 4% chord for negative and positive yaw cases and bin averaged results. Again, all surface pressure data were normalized with respect to the tip velocity. Figure 24 shows a -26.5-deg yaw case. In general, maximum suction pressures occurred as the blade reached maximum height (0-deg and 360-deg azimuth). At 180-deg azimuth, minimum suction pressures were encountered. These data exhibit an interesting spanwise distribution, however. From 30% - 47% span, there is an appreciable decrease in suction pressure. From 47% - 63% span, there was an increase in suction pressure that leveled off from 63% - 80% span. In addition, at 30% span, there appeared no evidence of a tower induced vortex (which would likely occur near 180-deg azimuth) but this vortex did appear in the pressure signature near 63% span and outboard locations. Figure 25 shows a spanwise pressure distribution for the 30-deg yaw case. As expected, maximum suction pressures occurred approximately 180 deg out of phase compared with the negative yaw case. There is no evidence of a tower induced vortex in the pressure profile except at 80% span. A constant pressure ridge does persist at approximately 200-deg azimuth along the entire span, possibly indicating uniform vortex initiation. However, the suction pressure peak persists for a relatively short while at 30% span and persists longer at outboard stations. At 80% span, in fact, the suction pressure maxima persist over 45 deg of the rotation cycle.

Figure 26 is identical to Figure 25 except single cycle rather than bin-averaged results are presented. In general, the trends are identical to the bin-averaged results with a few exceptions. The overall suction pressures are higher for single cycle results. Turbulence levels, exhibited by random pressure fluctuations, appeared greater and this turbulence increased at outboard stations.

Surface pressure distributions demonstrated the presence of discrete vortex structures. Convection of these vortex structures was evidenced by the temporal delay in maximum suction pressures downstream along the chord and were consistent with pressure signatures produced by vortex formations on pitching airfoils. Future analysis is required, however, to more accurately predict the formation of vortex structures on rotating wind turbines. This will allow for better modeling of structural loading and power generation.

Conclusions

Dynamic stall was shown to exist on a HAWT operating at a 30-deg yaw angle. Dynamic stall also occurs for low yaw error operation when tower shadow, wind shear, or inflow turbulence cause large AOA excursions. These increased aerodynamic loads cause increased structural loading. It was shown that dynamic stall forces, caused by tower shadow, are short in duration and lower in magnitude compared to those caused by yawed flow. It is important to model dynamic stall for yawed rotors for this reason. The data presented in this report plus future data will provide the basic information needed to develop dynamic stall models.

Future Work

Blade geometry appears to affect airfoil performance. To understand the effect of blade twist and taper on airfoil stall performance, a tapered and twisted blade will be developed and tested. Results will be compared to the existing blade, which has no twist or taper.

The flow conditions adjacent to the blade but off the surface (outer flow condition) may reveal the cause of airfoil performance abnormality. These flow states can be tested by observing smoke flow patterns as the blade is rotating through the smoke. Video cameras will be used to record these smoke patterns. Video image processing will be used to correlate the patterns with pressure distributions and other operating conditions. This information will be used to improve stall models for wind turbines.

References

1. Butterfield, C.P., D.A. Simms, W.P. Musial, G.N. Scott, Spanwise Aerodynamic Loads on a Rotating Blade, SERI/TP-257-3983, UC Category: 261, DE91002101, Wind Power '90 (October 1990).

2. Musial, W., and C.P. Butterfield, A Comparison of Two- and Three- Dimensional S809 Airfoil Properties for Rough and Smooth HAWT Rotor Operation, SERI/TP-257-3603, UC Category: 261, DE89009512, American Society of Mechanical Engineers (January 1990).

3. Viterna, L.A., and R.D. Corrigan, Fixed Pitch Rotor Performance of Large Horizontal Axis Wind Turbines, DOE/NASA Workshop on Large Horizontal Axis Wind Turbines, Cleveland, Ohio (July 28-30, 1981).

4. Butterfield, C.P., Three-Dimensional Airfoil Performance Measurements on a Rotating Wing, SERI/TP-217-3505, Solar Energy Research Institute, Golden, CO (June 1989).

5. Wright, A., and C.P. Butterfield, The SERI Teetering Hub Rotor Code: Final Results and Conclusions, Wind Power 91, Palm Springs, CA (September 1991).

6. Hansen, A.C., and C.P. Butterfield, "Yaw Loads and Motions of a Horizontal Axis Wind Turbine," ASME Journal of Solar Energy, Vol. 112 (November 1990).

7. Butterfield, C.P., and E. Nelsen, Aerodynamic Testing of a Rotating Wind Turbine Blade, SERI/TP-257-3490, Solar Energy Research Institute, Golden, CO (January 1990).

8. Butterfield, C.P., M. Jenks, D. Simms, and W. Musial, Aerodynamic Pressure Measurements on a Rotating Wind Turbine Blade, SERI/TP-257-3695, Solar Energy Research Institute, Golden, CO (May 1990).

9. Tangler, J., and D. Somers, Status of the Special Purpose Airfoil Families, SERI/TP-217-3264, Solar Energy Research Institute, Golden, CO (December 1987).

10. Somers, D.M., Design and Experimental Results for the S809 Airfoil, March 1989 (to be published)

11. Gregorek, G.M. (unpublished report of OSU testing of S809, November 1989).

12. Butterfield, C.P., G. Scott, and W. Musial, Comparison of Wind Tunnel Airfoil Performance Data with Wind Turbine Blade Data, SERI/TP-254-3799, Solar Energy Research Institute, Golden, CO (July 1990).

13. Robinson, M. C., Development of Vorticity and Vortices from Forced Unsteady Flow Separation, Ph.D. Thesis, University of Colorado, Boulder, CO (July 1985).

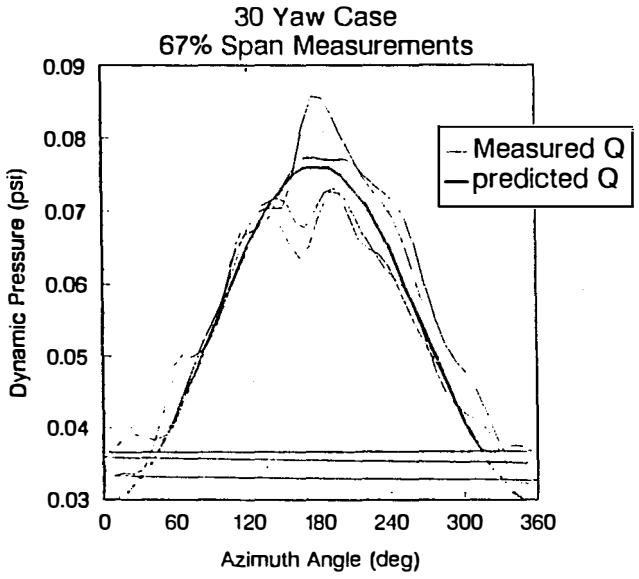

Figure 1. Dynamic pressure variations during yaw.

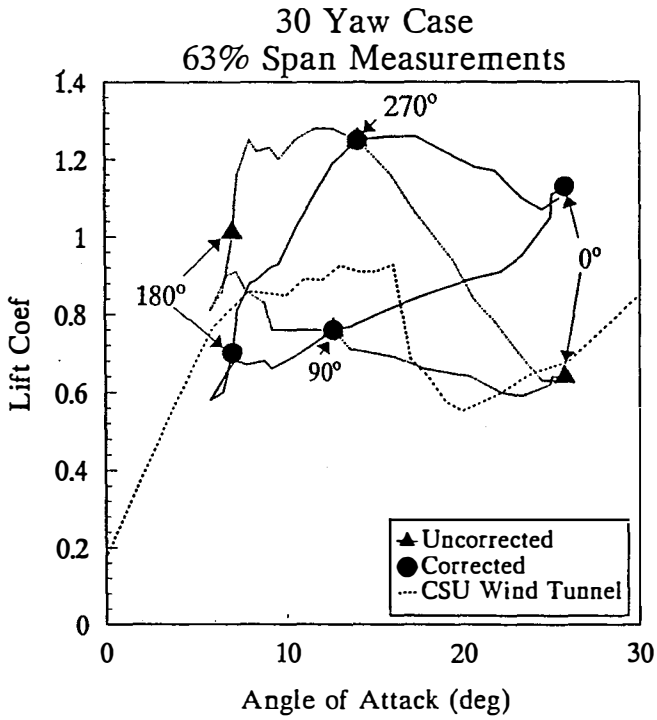

Figure 2. Effects of time-varying dynamic pressure normalization.

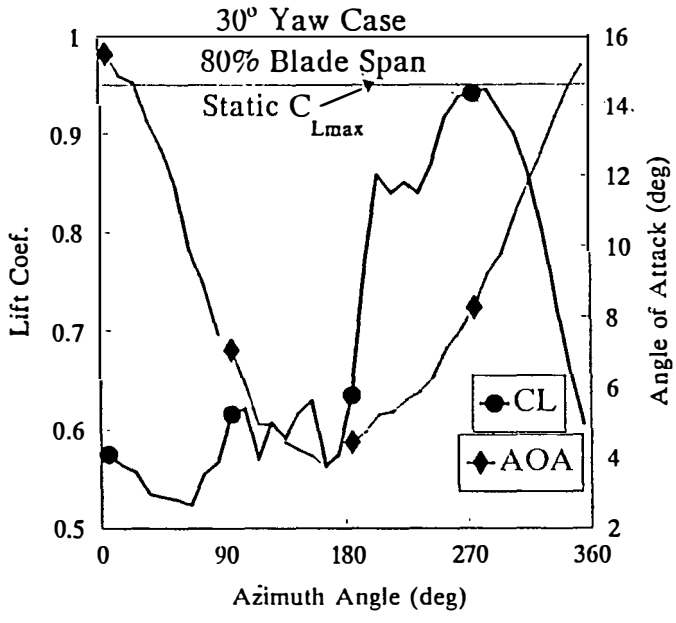

Figure 3. Azimuth-averaged AOA and lift coefficient at 80% span for 30-deg yaw case.

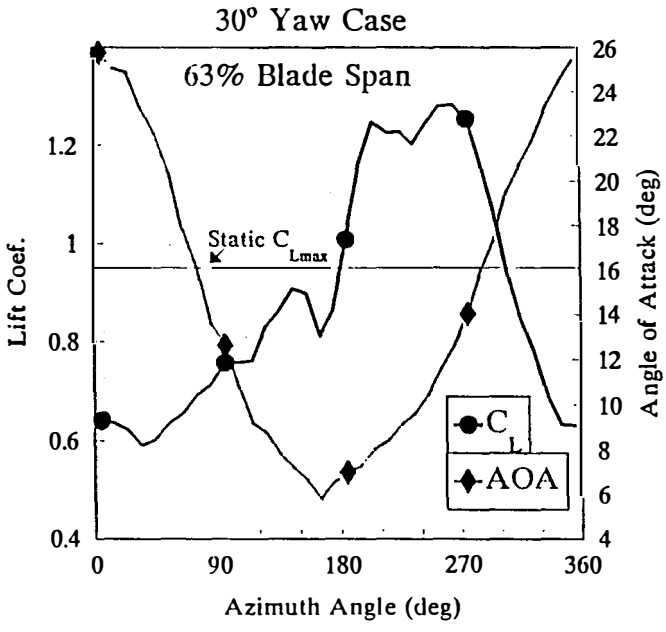

Figure 4. Azimuth-averaged AOA and lift coefficient at 63% span for 30-deg yaw case.

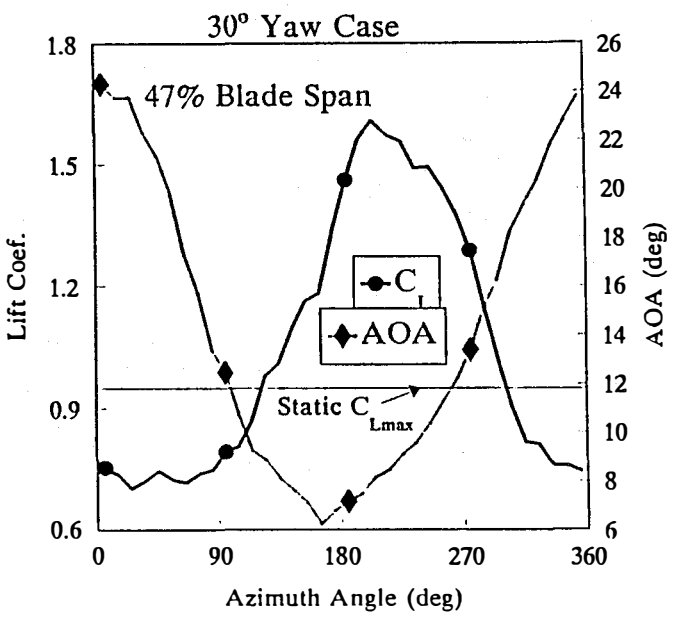

Figure 5. Azimuth-averaged AOA and lift coefficient at 47% span for 30-deg yaw case.

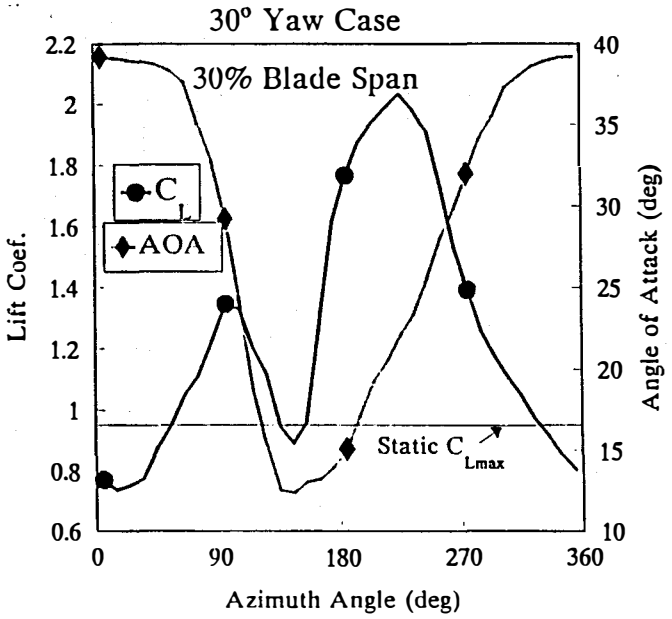

Figure 6. Azimuth-averaged AOA and lift coefficient at 30% span for 30-deg yaw case.

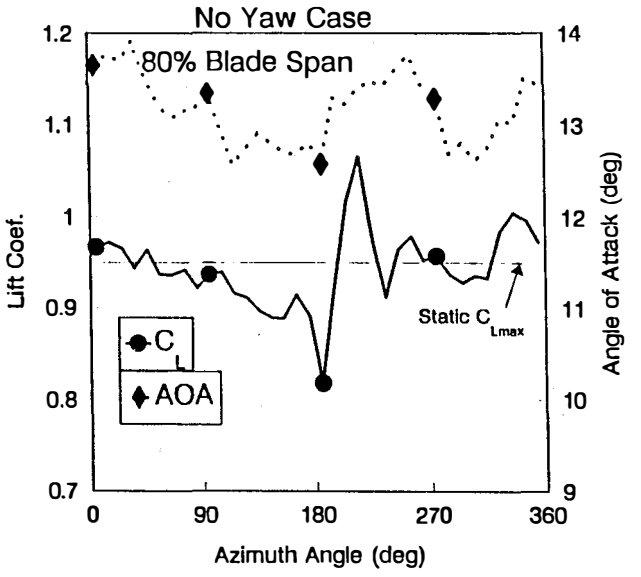

Figure 7. Azimuth-averaged AOA and lift coefficient at the 80% span for no yaw case.

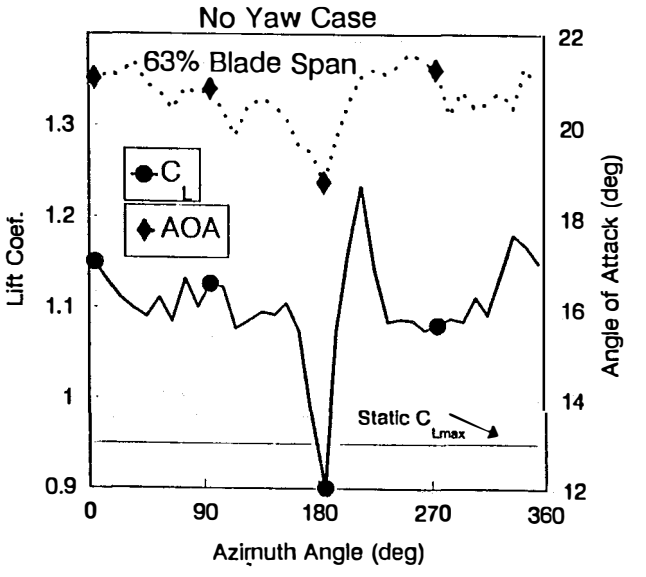

Figure 8. Azimuth-averaged AOA and lift coefficient at 63% span for no yaw case.

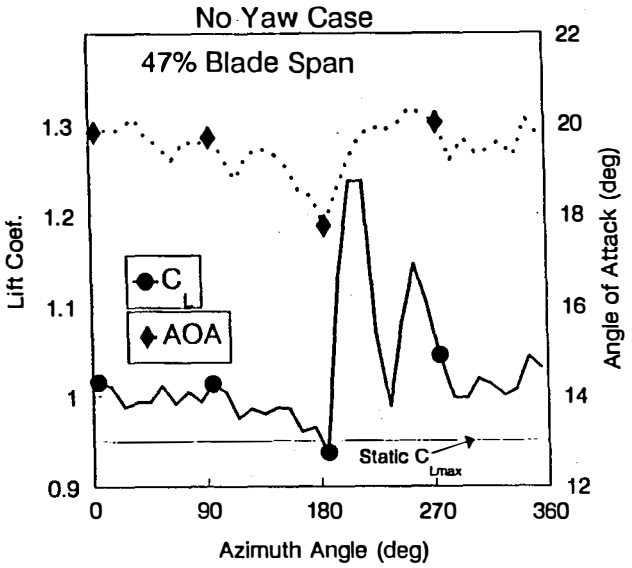

Figure 9. Azimuth-averaged AOA and lift coefficient at 47% span for no yaw case.

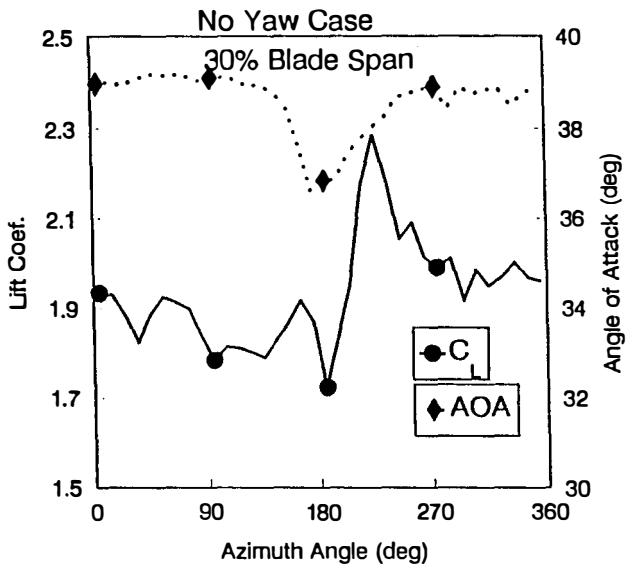

Figure 10. Azimuth-averaged AOA and lift coefficient at 30% span for no yaw case.

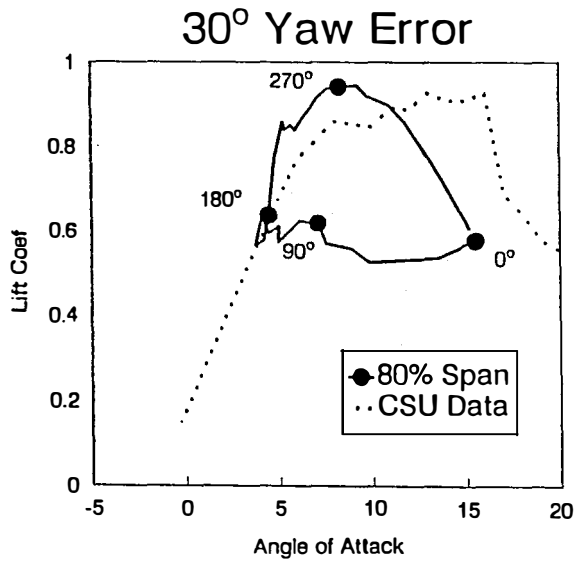

Figure 11. Dynamic stall at 80% span.

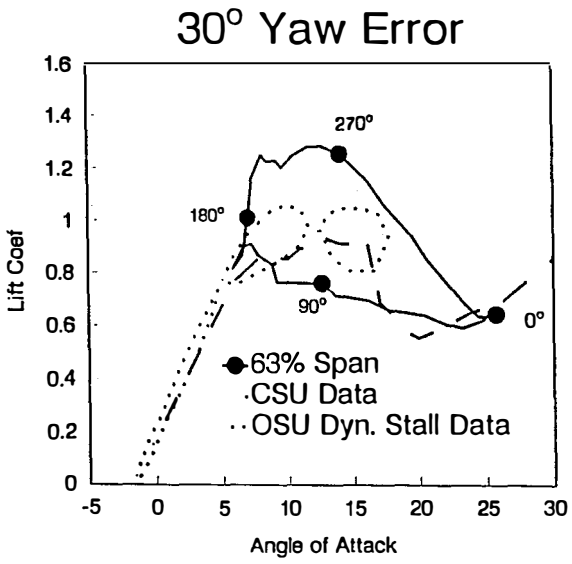

Figure 12. Dynamic stall at 63% span compared to wind tunnel dynamic stall.

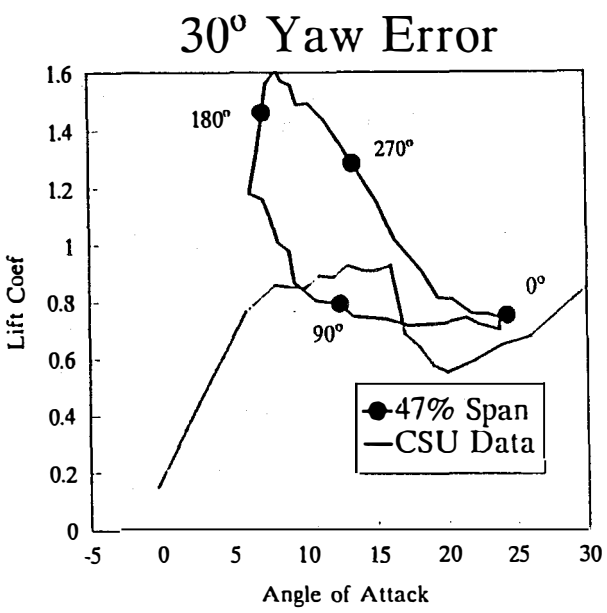

Figure 13. Dynamic stall at 47% span.

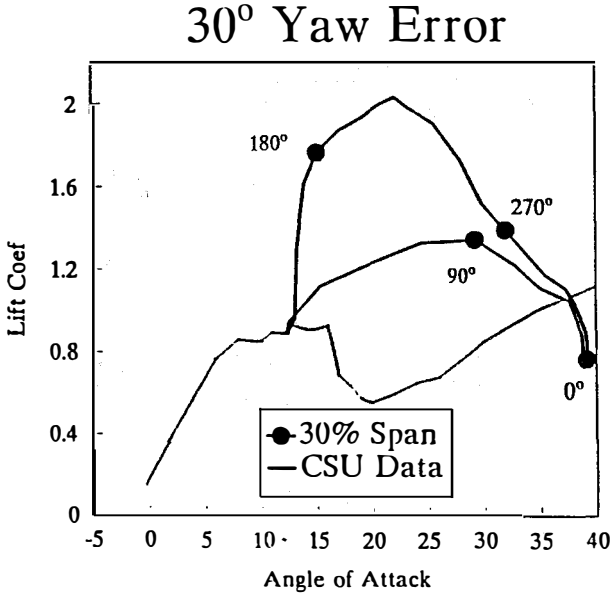

Figure 14. Dynamic stall at 30% span.

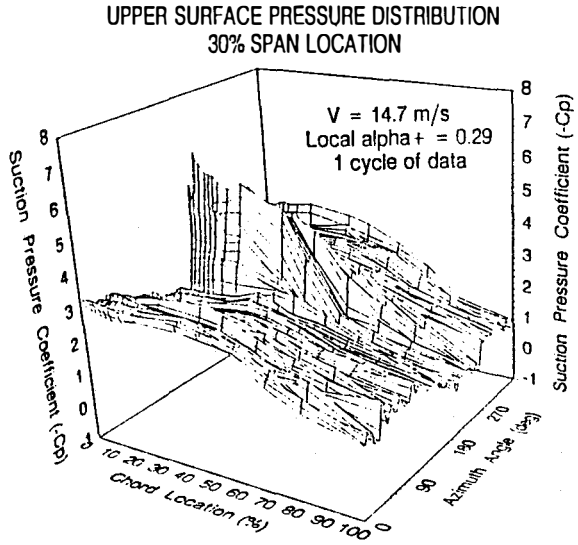

Figure 15. Chordwise surface pressure distribution versus azimuth angle, V = 14.7 m/s, 0-deg yaw, 30% span, one cycle of data.

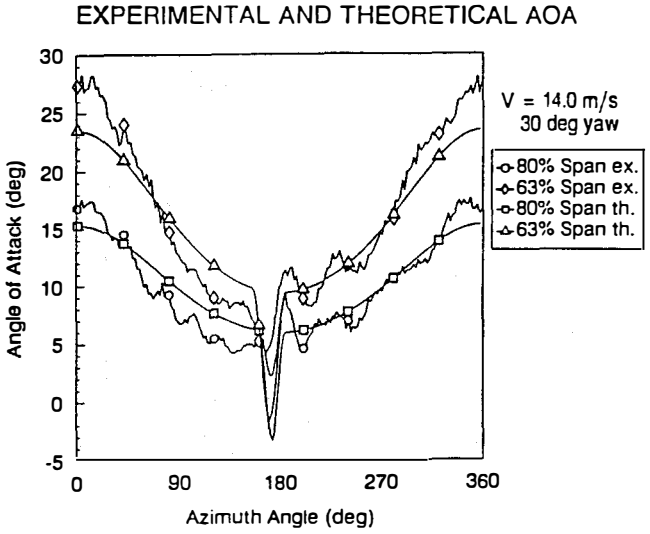

Figure 16. Measured and geometric local AOA versus azimuth angle.

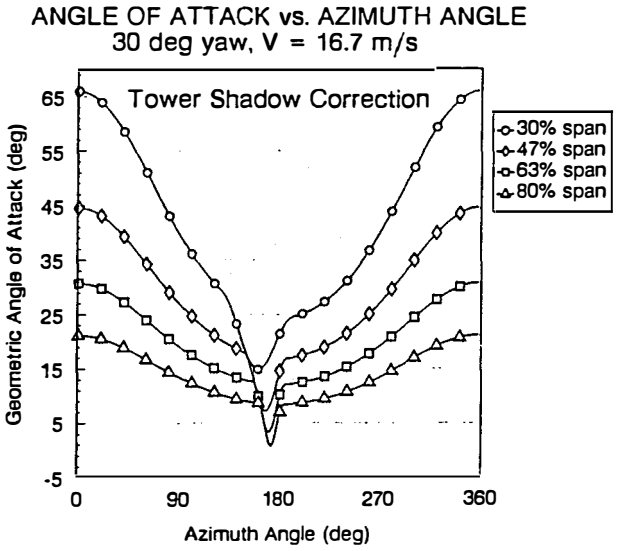

Figure 17. Theoretical geometric AOA versus azimuth angle, 30-deg yaw, V = 16.7 m/s.

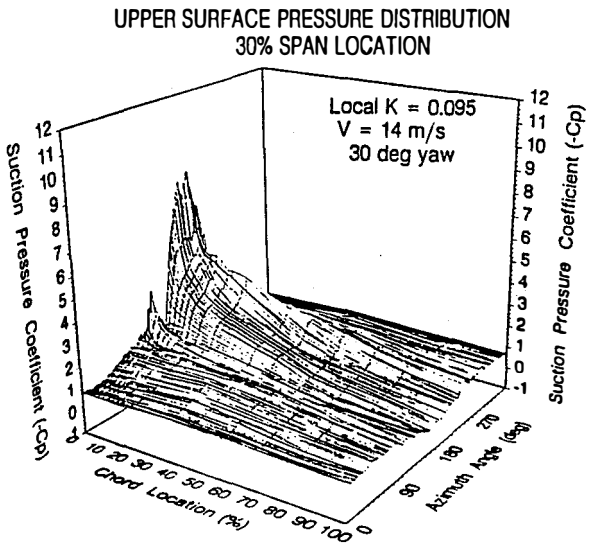

Figure 18. Chordwise surface pressure distribution versus azimuth angle, 30-deg yaw, V = 14 m/s, 30% span, bin-averaged data.

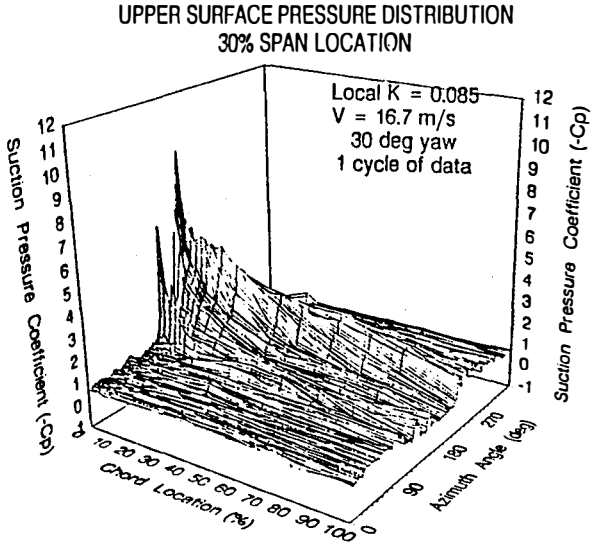

Figure 19. Chordwise surface pressure distribution versus azimuth angle, 30-deg yaw, V = 16.7 m/s, 30% span, one cycle of data.

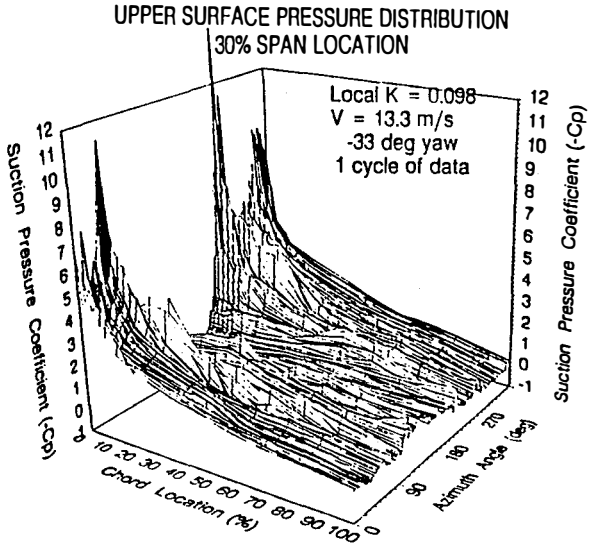

Figure 20. Chordwise surface pressure distribution versus azimuth angle, -33-deg yaw, V = 13.3 m/s, 30% span, one cycle of data.

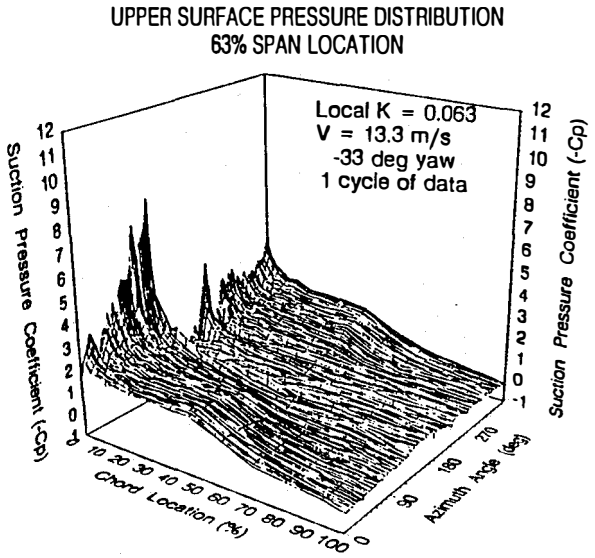

Figure 21. Chordwise surface pressure distribution versus azimuth angle, -33-deg yaw, V = 13.3 m/s, 63% span, one cycle of data.

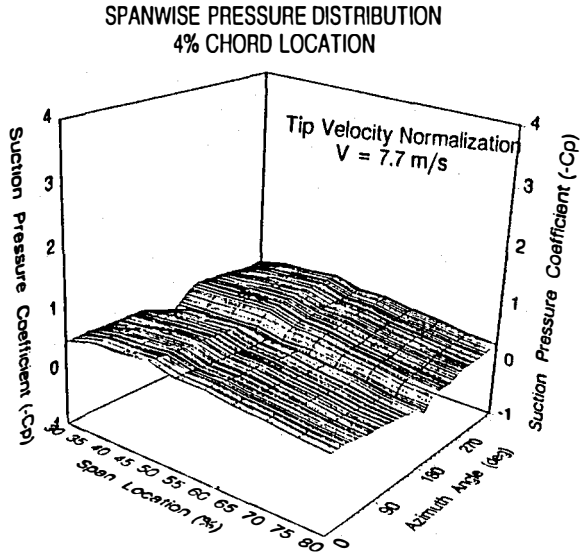

Figure 22. Spanwise pressure distribution versus azimuth angle, 7.7 m/s wind speed, 4% chord, tip velocity normalization, bin-averaged data.

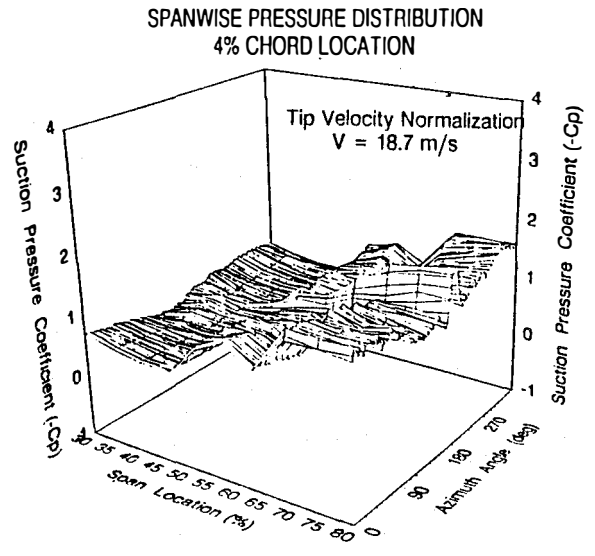

Figure 23. Spanwise pressure distribution versus azimuth angle, 18.7 m/s wind speed, 4% chord, tip velocity normalization, bin-averaged data.

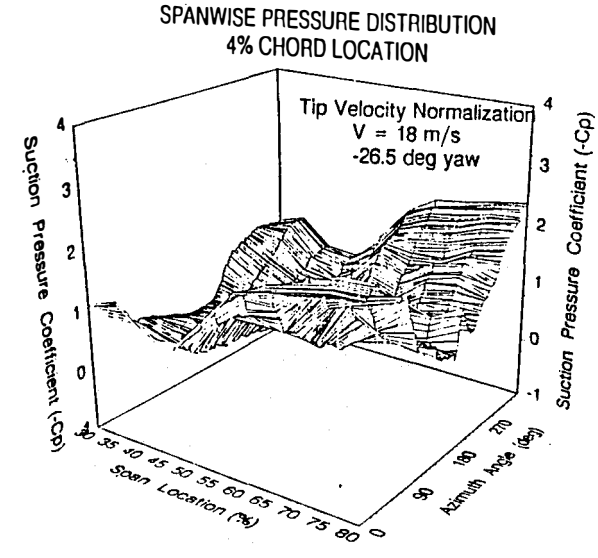

Figure 24. Spanwise pressure distribution versus azimuth angle, 18 m/s wind speed, 4% chord, tip velocity normalization, bin-averaged data, -26.5-deg yaw.

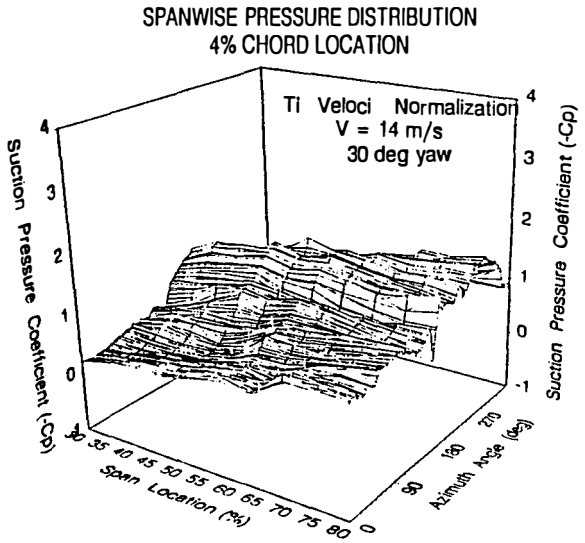

Figure 25. Spanwise pressure distribution versus azimuth angle, 14 m/s wind speed, 4% chord, tip velocity normalization, bin-averaged data, 30-deg yaw.

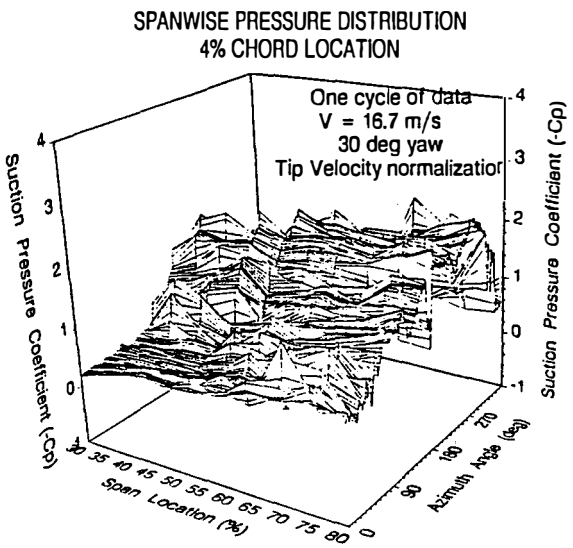

Figure 26. Spanwise pressure distribution versus azimuth angle, 16.7 m/s wind speed, 4% chord, tip velocity normalization, bin-averaged data, 30-deg yaw.